J. Synchrotron Rad. (1998). **5**, 1243–1249

Conserving the Coherence and Uniformity of Third-Generation Synchrotron Radiation Beams: the Case of ID19, a 'Long' Beamline at the ESRF

José I. Espeso,[a,b] Peter Cloetens,[a,c]* José Baruchel,[a] Jürgen Härtwig,[a] Trevor Mairs,[a] Jean Claude Biasci,[a] Gérard Marot,[a] Murielle Salomé-Pateyron[a,d] and Michel Schlenker[e]

[a]European Synchrotron Radiation Facility, BP 220, F-38043 Grenoble CÉDEX, France, [b]Universidad de Cantabria, Santander, Spain, [c]EMAT, University of Antwerp, B-2020 Antwerpen, Belgium, [d]CREATIS, INSA, F-69621 Villeurbanne CÉDEX, France, and [e]Laboratoire Louis Néel, CNRS, F-38042 Grenoble CÉDEX, France. E-mail: cloetens@esrf.fr

(*Received 17 November 1997; accepted 5 February 1998*)

The lateral coherence length is of the order of 100 μm at the 'long' (145 m) ID19 beamline of the ESRF, which is mainly devoted to imaging. Most of the optical elements located along the X-ray path can thus act as 'phase objects', and lead to spurious contrast and/or to coherence degradation, which shows up as an enhanced effective angular size of the source. Both the spurious contrast and the coherence degradation are detrimental for the images (diffraction topographs, tomographs, phase-contrast images) produced at this beamline. The problems identified and the way they were solved during the commissioning of ID19 are reported. More particularly, the role of the protection foils located in the front end, the beryllium windows, the filters and the monochromator defects (scratches, dust, small vibrations) is discussed.

Keywords: X-ray coherence; phase-sensitive imaging; monochromators; filters; windows.

1. Introduction

The spatial coherence of synchrotron radiation X-ray beams has recently been shown to provide novel physical information both in diffraction ('speckle') (Sutton *et al.*, 1991; Brauer, Stephenson, Sutton, Brüning *et al.*, 1995) and in imaging ('phase contrast') experiments (Snigirev *et al.*, 1995; Cloetens *et al.*, 1996). The images are particularly sensitive to the beam coherence properties at the beamlines of small-emittance machines such as the ESRF. The lateral coherence length, $\lambda/2\alpha$, is inversely proportional to α, the angular size of the X-ray source as seen from the sample position. This divergence α is only 0.1 to 1 μrad at ID19, the first operational 'long' beamline of the ESRF, due to both the very small source size reached on this third-generation synchrotron radiation facility and the length of this beamline. The divergence and the lateral coherence length have different values in the vertical and horizontal directions due to the anisotropic shape of the source.

Spurious images from beryllium windows have been reported (Cloetens *et al.*, 1996; Snigirev *et al.*, 1996), indicating that nearly everything along the X-ray path can act as a phase object, and lead to degradation of the beam quality. This degradation is unacceptable for critical applications such as (coherent) imaging, X-ray focusing, dispersive EXAFS studies and high-resolution diffraction. The aim of this paper is to report the problems encountered and the actions taken at the beamline in order to retain a homogeneous beam and good coherence. The causes of loss of uniformity and coherence were found to be the protection foils located in the front end, the beryllium windows, the filters and the monochromators. After describing the experimental set-up, we will discuss the measures taken to alleviate the problems related to each element. Measurement of the spatial coherence was performed either by recording the Fresnel fringes from an edge or a fibre (Cloetens *et al.*, 1996; Schelokov *et al.*, 1996) or by using a periodic phase object and measuring the variation of the image contrast at equivalent 'Talbot' positions (Cloetens, Guigay, de Martino, Baruchel & Schlenker, 1997).

2. Experimental set-up

The ID19 beamline went into operation in June 1996. It is mainly devoted to imaging, more particularly to Bragg-diffraction imaging (X-ray topography), and to absorption and phase-sensitive radiography. Its main features (Baruchel *et al.*, 1993) derive from the requirements of delivering a spectrally and spatially homogeneous X-ray beam at the sample position, with dimensions 40 × 14 mm, with high photon flux and a tunable photon energy (10–120 keV). These requirements led to the choices of a long (145 m)

beamline and an 11-pole variable-field wiggler (B_{max} = 1.4 T, K_{max} = 20). The wiggler is situated in a low-β section of the storage ring with nominal values of the electron beam size of 20 μm vertically and 150 μm horizontally. Either a spectrally continuous beam, containing a substantial part of the synchrotron radiation X-ray spectrum (white beam), or a monochromatic beam can be used in the experimental hutch. The monochromatic beam is delivered by either of two types of monochromator. The horizontal monochromator, located in the experimental hutch, 145 m from the source, consists of a single crystal diffracting in the horizontal plane. The vertical monochromator is a fixed-exit double-crystal system located in a vacuum enclosure in the monochromator hutch, 140 m from the source. The sample is set on a diffractometer which can move on air pads on the marble floor of the experimental hutch. Either a cooled CCD camera, with low noise and fast readout that was developed at the ESRF (Labiche *et al.*, 1996) and equipped with visible-light optics and scintillators, or high-resolution film (Kodak SO-343) are used as imaging detectors, with resolutions ranging from 1 to 10 μm.

The features of ID19 make it well adapted for imaging objects which only affect the phase of the X-ray beam passing through them, without local variations in the attenuation, with a simple technique based on free-space propagation. Here, a two-dimensional detector is set at a finite distance (of the order of 1 m) from the specimen, whereas this distance is kept as small as possible for absorption radiography. The physical principle involved is Fresnel diffraction and this technique is similar to the defocusing mode of electron microscopy and to in-line Gabor holography in optics. This 'propagation' technique has already been successfully applied to the imaging of objects with negligible absorption for hard X-rays but appreciable variations in optical path length. Examples of the latter are two- or three-dimensional (tomographic) phase-sensitive images of biological (plants, soft tissues *etc.*) or artificial (crystals, composites or ceramics with inclusions, holes, cracks *etc.*) materials (Cloetens, Pateyron-Salomé *et al.*, 1997). Three-dimensional reconstruction can be performed either directly with a filtered back-projection algorithm, initially designed for processing attenuation images but which was shown to be a workable approximation in some cases (Cloetens, Pateyron-Salomé *et al.*, 1997), or in combination with a phase-reconstruction procedure similar to that used for electron microscopy (Cloetens, Guigay, de Martino, Salomé, Schlenker & Van Dyck, 1997). The propagation technique is being extended to the *in-situ* investigation of crack formation and propagation in metal-matrix composites as a function of stress (Buffière *et al.*, 1997).

Any object in the X-ray beam that is not completely uniform in density and thickness will, if it is an appreciable distance upstream of the detector, also produce a (spurious) image. The phase modulation introduced by this non-uniformity is given by

$$\varphi(x, y) = \int [2\pi n(x, y, z)/\lambda]\, dz, \quad (1)$$

where the z axis is chosen along the mean direction of the beam and $n(x,y,z)$ denotes the real part of the refractive index distribution in the sample. This latter quantity depends on the material composition through

$$n = 1 - (r_e\lambda^2/2\pi V)\sum(Z_i + f_i'), \quad (2)$$

where r_e = 2.8 fm is the classical electron radius, the summation is over all the atoms contained in volume V, Z_i is their atomic number and f_i' is the real part of the wavelength-dependent dispersion correction. The value of $1 - n$ is very small ($\sim 10^{-6}$) in the hard X-ray range. It can be easily shown that, to a good approximation, $1 - n$ is proportional to $\Delta\rho$, the variation in material density ρ. The 'image' depends strongly on the effective defocusing distance,

$$D = z_1 z_2/(z_1 + z_2), \quad (3)$$

where z_1 and z_2 denote the source–sample and sample–detector distances, respectively. In the case $z_1 >> z_2$, D is approximately equal to the sample–detector distance. The observed pattern (Guigay, 1977; Pogany *et al.*, 1997) is strongly sensitive to spatial frequencies in the phase modulation corresponding to a distance a given by

$$a = (2\lambda D)^{1/2}, \quad (4)$$

and includes a magnification, M, given by

$$M = (z_1 + z_2)/z_1, \quad (5)$$

which is equal to unity in the case of a very distant source. In the case of a weak phase object it can be shown that the intensity modulation is of the order of the phase modulation expressed in radians (Snigirev *et al.*, 1995).

The finite source size, s, results in a partially coherent beam (Guigay, 1977) and limits the resolution, r, in the detector plane. The geometrical resolution for an incoherent source is given by

$$r = sz_2/z_1 = z_2\alpha, \quad (6)$$

and will have a different value in the vertical and horizontal directions.

3. Optical elements

ID19 has a 150 mm period wiggler of relatively low power density but rather large total power (>1 kW). The first beryllium window, separating the vacuum of the storage ring and the beamline, has low absorption for hard X-rays, but not in the soft part of the synchrotron radiation spectrum. Its cooling system is unable to dissipate the corresponding heat load. This window must therefore be protected by a filter. In most of the similar ESRF beamlines, two 0.25 mm-thick pyrocarbon foils are placed just before the beryllium window, *i.e.* 25 m from the source. Fig. 1(*a*) shows an image of a monochromatic beam obtained from a flat Si(111) crystal diffracting, in symmetrical Bragg setting, in the horizontal plane, at 145 m from

the source (photon energy 20 keV). A wavy structure and horizontal lines are clearly visible. To isolate the problem, all beamline beryllium windows were replaced with polished aluminium. Most of the structure was still present, and thus was originating from the elements (pyrocarbon foils and the remaining beryllium window) located in the front end. The horizontal lines were known to originate from the beryllium, as will be discussed in more detail later. Therefore, it was suggested that the diagonal lines were originating from the pyrocarbon filters. This was easily confirmed in Fig. 1(*b*) by a test performed when the machine was operated at a low enough current to be safe (<100 mA) for operation without carbon filters. Another filtering material was required for usual operation. Using the propagation technique in our experimental hutch (sample-to-detector distance in the 1–4 m range), we tested several other possibilities. The observed wavy images appear to mainly correspond to internal density inhomogeneity, and polishing the foil does not improve the situation. Highly oriented pyrolitic graphite (HOPG) introduces less pronounced spurious images, but is still not satisfactory. Diamond plates produced by chemical vapour deposition (CVD) appeared to be more promising. The specification of the plates was as follows: thickness 250 ± 25 μm, surface finish 0.03 μm r.m.s., maximum peak-to-valley distance 0.4 μm, optical grade. Fig. 2 shows that no phase image was introduced when a diamond plate was placed into the monochromatic beam. Indeed, since the ID19 beam was far from homogeneous at that time, it was only possible to detect the differences in behaviour with and without diamond. There were no general contrast features added to the image, but some occasional intensity drops. This local loss of intensity was assigned to Bragg diffraction from individual crystallites. When the diamond plate is rotated, the location and shape of the diffracting crystallites change, but their number and average size (50–100 μm) remain. Several diamonds, produced by the CVD technique but provided by different suppliers, were tested. All of them display basically the same features. Nevertheless, the diamond plates were a large improvement with respect to the graphite foils, and were installed in the front end. The local loss of intensity with these new protection filters located at 25 m from the source and at 120 m from the sample, though still observable (10% over about 0.1 mm^2), is less dramatic than in Fig. 2 because of the blurring associated with the source size.

Figs. 1(*a*) and 1(*b*) show two sets of horizontal lines. They were traced to slight rolling defects in the two beryllium windows placed across the beamline at 26 m from the source (wide lines in Fig. 1*b*) and 135 m from the source (fine lines in Fig. 1*a*). At the photon energy used, the absorption of the beryllium windows is negligible, and these images are due to the variations in optical path length, *i.e.* of phase, associated with the variations in thickness (∼5 μm). The width of the lines, about 380 μm and 45 μm, respectively, can be understood from the respective values of the defocusing distance D (21 m and 9.3 m, respectively) and magnification (about 6 and 1, respectively). This type

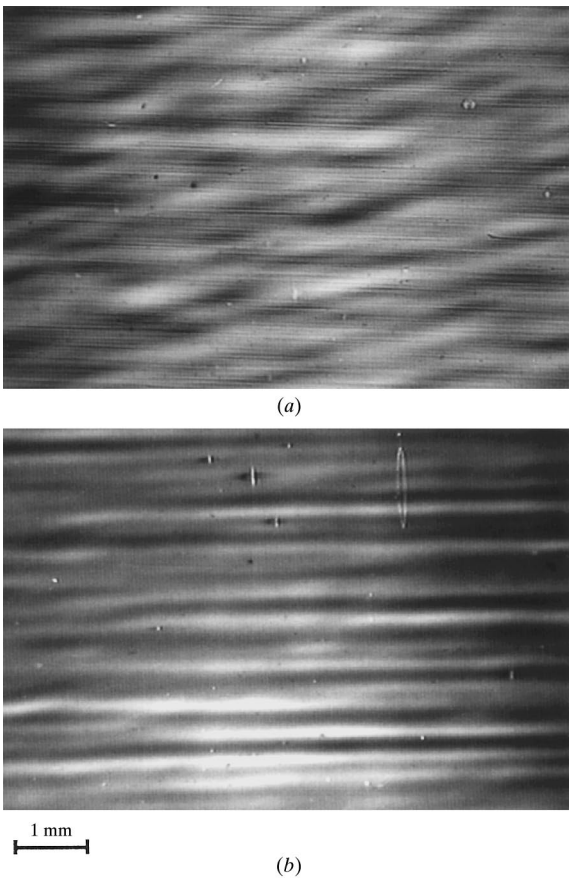

(*a*)

(*b*)

Figure 1
Image of a monochromatic beam obtained from a flat Si(111) crystal diffracting, in symmetrical Bragg setting, in the horizontal plane, at 145 m from the source (E = 20 keV). (*a*) Lines, due to the beryllium windows located at 26 and 135 m from the source, and a wavy structure, associated with the carbon filters located at 25 m with respect to the source, are clearly visible. (*b*) The same image after removing the second beryllium window and the carbon filters.

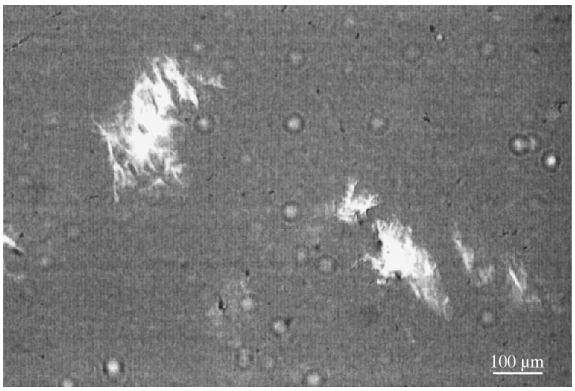

Figure 2
Image of a monochromatic beam after passage through a CVD-grown diamond plate. No diamond-related spurious phase images are observed, but local dips in the intensity are associated with Bragg diffraction by diamond crystallites (50–100 μm). The sample–detector distance was 2.4 m at an X-ray energy of 20 keV.

of artefact can be removed by using a 'random phase plate' (Cloetens *et al.*, 1996), which consists of a rotating inhomogeneous material. However, the use of such a device increases the incident divergence and reduces dramatically the beam coherence.

Several polished beryllium windows were tested in order to replace the defective ones. Fig. 3 shows that fringe visibility in the Fresnel diffraction pattern of a fibre is not altered when the circular Be window, which was later used for the front end, was inserted into the monochromatic beam. The presence of the window is only revealed by the edge contrast occurring at its border. This beryllium is Brush-Wellman grade PF60, with a specification of 0.02 μm r.m.s. and an actual measured figure of 0.01 μm on both faces. Sealing the beryllium to its copper flange was performed in this case with gold wire.

It should be noted that just giving the polishing specification as the r.m.s. roughness is not enough for an imaging beamline: a single scratch will scarcely modify the r.m.s., but is very detrimental for the image quality. The beryllium windows appeared to be satisfactory and, to fulfil our requirements, were polished by the SAGEM company, and, for some of them, brazed by METACERAM. The r.m.s. value was specified to be less than 0.02 μm, and the peak-to-valley roughness to be less than 0.1 μm, which corresponds to a phase modulation of 0.017 rad at an X-ray energy of 10 keV.

No mirror was included in the design of the beamline because tests performed at the optics beamline (BM5) showed that, at that time, the state-of-the-art mirrors produced a rather inhomogeneous beam (Schelokov *et al.*, 1996). The selection of the energy bandwidth in the white beam, suited to a given experiment, can nevertheless be performed by adjusting the wiggler gap and by inserting appropriate filters.

These filters, located about 30 m from the source, are therefore vital elements for beamline operation. They must be internally homogeneous and carefully polished because any weak but abrupt variation in thickness (scratch, etch pit *etc.*) produces a phase-contrast image. Figs. 4(*a*) and 4(*b*) show the images obtained without and with a 1 mm-thick aluminium filter, respectively. In this first attempt the filter was manually polished. Good results were obtained later by

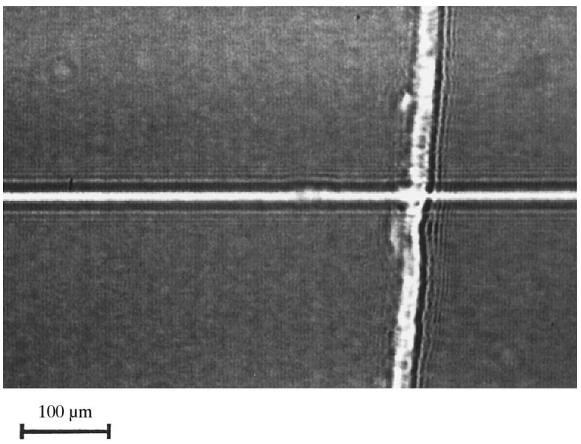

Figure 3
Phase image of a polymer fibre, 13 μm in diameter, and of a circular Be window: the Fresnel fringes from the fibre are not affected by the presence of this polished beryllium plate, which was later used as the front-end window of the beamline. The plate covers the left part of the image. The sample–detector distance was 2.3 m and 2.8 m for the fibre and the plate, respectively, at $\lambda = 0.7$ Å.

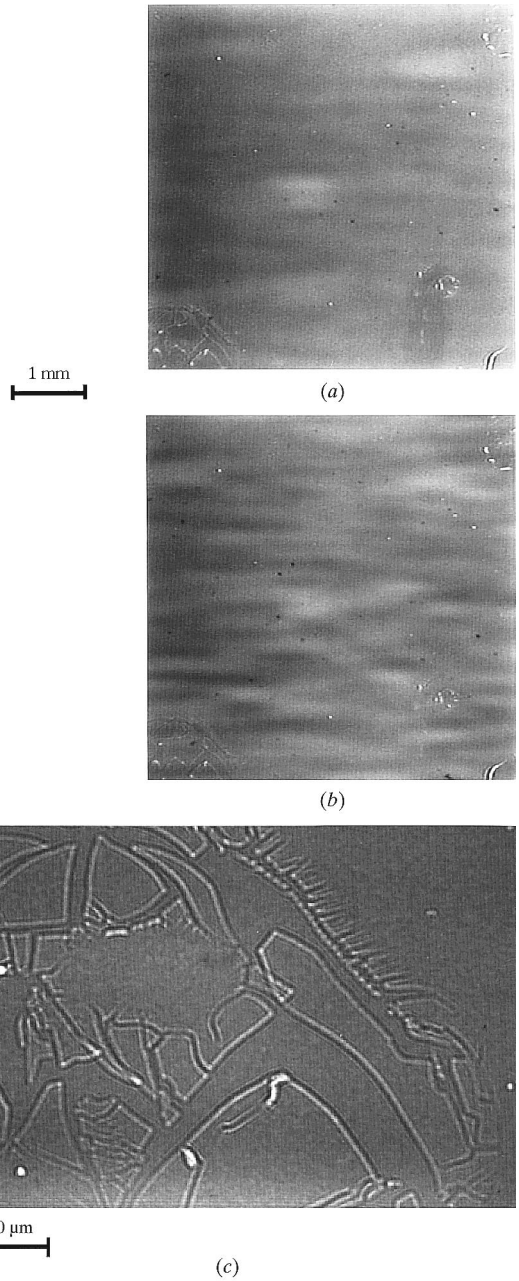

Figure 4
Images of a monochromatic beam (*a*) without and (*b*) with a 1 mm-thick aluminium filter located at 30 m from the source show spurious images, which were removed by a further very accurate polishing; (*c*) magnified image of an oxidized part of the last aluminium filter, located in the experimental hutch at a distance of 143 m from the source and 2 m from the detector; X-ray wavelength 0.7 Å.

polishing the aluminium with the same mechanochemical technique as for silicon crystals. Fig. 4(*c*) shows a spot occurring on both Figs. 4(*a*) and 4(*b*), corresponding to an area of oxidation of the last aluminium filter, located in the experimental hutch.

The vertical as well as the horizontal monochromators are based on the use of perfect silicon crystals, mechanochemically polished, set for reflection 111 in symmetrical Bragg geometry. This setting is the only one which does not introduce an extra divergence of the beam, and consequently a degradation of the coherence properties (H. Chen & M. Kuriyama, unpublished; Brauer, Stephenson, Sutton, Mochrie *et al.*, 1995). Fig. 5 is a graphical representation, based on the dispersion surface approach, of this fact. It is well known that the classical Huygens–Snell construction allows one to determine, when knowing the dispersion surface and the incident plane wave in a vacuum, which wavefields propagate into the crystal, and what waves come out from the crystal (Authier, 1997). Fig. 5 shows the results of the same construction, restricted to the relevant small portions of the constant wavelength surfaces describing propagation in a vacuum. Fig. 5(*a*) describes the symmetrical Bragg setting and Fig. 5(*b*) describes the symmetrical Laue case. In fact, two sets of vacuum surfaces are represented in each figure, corresponding to two energies (different lengths of the wavevectors $\mathbf{k}_{o1}$ and $\mathbf{k}_{o2}$) within the acceptance bandwidth of the crystal. A comparison of Figs. 5(*a*) and 5(*b*) shows that, when $\mathbf{k}_{o1}$ and $\mathbf{k}_{o2}$ lie along the same direction, this is also the case for $\mathbf{k}_{h1}$ and $\mathbf{k}_{h2}$ in the symmetrical Bragg case (Fig. 5*a*), whereas the Laue case introduces an extra divergence (Fig. 5*b*). This divergence corresponds to the finite bandwidth diffracted by the crystal. It can be corrected when using a second reflection with opposite asymmetry in the $(+n,-n)$ setting.

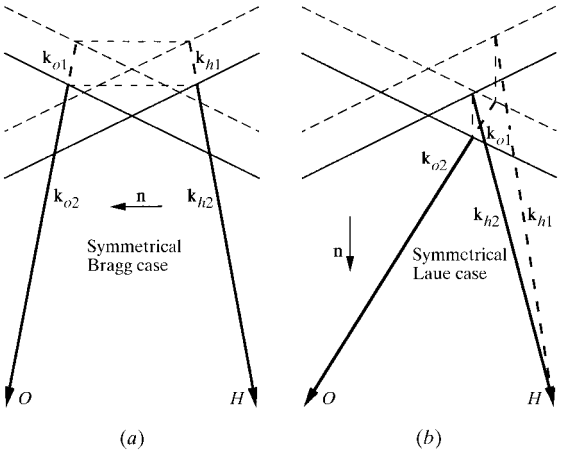

Figure 5
Vacuum surfaces for two wavelengths within the bandwidth corresponding to the intrinsic diffraction width of the monochromator in the (*a*) symmetrical Bragg and (*b*) symmetrical Laue cases. It can be observed that an additional divergence with respect to the incoming beam occurs in the diffracted beam in the Laue case but not in the symmetrical Bragg one.

The monochromatic beam is very sensitive to irregularities on the monochromator surfaces. These include dust, which is difficult to completely eliminate, as well as faint scratches. Fig. 6(*a*) shows the 'butterfly'-like contrast of a dust particle deposited on the monochromator. This double contrast can be easily understood when considering that the dust particle introduces a phase shift both on the incoming (direct) beam and on the diffracted beam (Schelokov *et al.*, 1996).

The usual requirement in conventional Bragg-diffraction imaging is that the surfaces of the investigated crystal (and/or monochromator) be strain free; no specific requirement is made on the flatness of the surface. This is no longer true when dealing with high-quality crystals and using a coherent X-ray beam. Fig. 6(*b*) shows an image of a surface scratch, which is mainly a phase-contrast image, the direct image component, associated with a gradient of distortion in the crystal (Authier, 1997), being very weak.

A specific problem arose due to the deposition of a thin layer (estimated to be a fraction of a micrometre thick from the colour rings observed in visible light) of hydrocarbon on the first monochromator crystal surface. Under the X-ray beam this deposit partly recombined with the silicon and introduced spurious phase images. This deposition

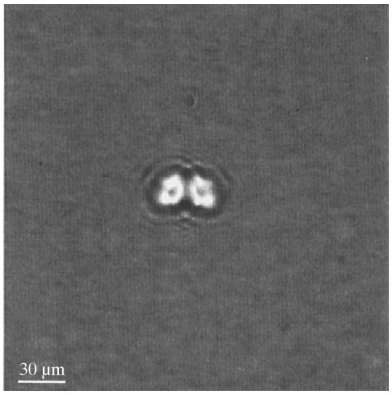

(*a*)

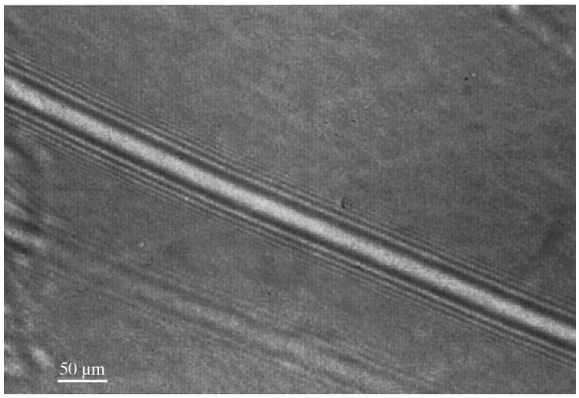

(*b*)

Figure 6
(*a*) 'Butterfly'-like contrast of a dust particle deposited on the horizontal monochromator; distance D = 1.5 m. (*b*) Phase image of a faint scratch on the Si(111) monochromator surface; distance D = 1 m. Symmetrical Bragg setting, λ = 0.7 Å.

process could be retarded after a modification of the cooling conditions and a substantial improvement of the vacuum at the position of the monochromator, making repolishing of the crystal less frequently necessary. Alternatively, when the monochromator is put under an inert helium atmosphere, contamination of the crystal surface is also avoided and the helium introduces only a slight increase in absorption and background.

Fig. 7 shows the DuMond diagram corresponding to the production of an 18 keV beam at the ID19 beamline using an Si(111) crystal in a symmetrical Bragg setting. The intrinsic diffraction width of this reflection is, at this energy, about 14 μrad, while the vertical angular size of the source seen from the monochromator is only 0.2 μrad. This implies that a vibration of 1 μrad does not affect the diffracted intensity, even when considering the diffraction by the second crystal (the diffraction curves of the first and second monochromator crystals superimpose in Fig. 7). However, this small vibration, indicated by dotted lines on the DuMond diagram, leads to an increase in the effective source size from 20 to 200 μm, or, correspondingly, to a drop in the lateral coherence length at wavelength λ = 0.69 Å from 250 to 25 μm.

Such a vibration was observed to be associated with the water cooling of the vertical monochromator. The water flow was calculated to be sufficient for the maximum beam size (14 × 40 mm^2) and minimum gap. When reducing the beam size or opening the gap, it is possible to reduce the flow by regulation of the water pressure. The effect of the vibrations was experimentally checked by verifying that the lateral coherence length is a decreasing function of the water pressure. The measurement was based on the images of a periodic object. Fresnel diffraction from a grating leads to the 'Talbot effect' which implies that the intensity distribution is periodic in both the y direction of the object periodicity (period a) and in the propagation direction (period $D_T = 2a^2/\lambda$) (Guigay, 1971; Cloetens, Guigay, de Martino, Baruchel & Schlenker, 1997). Fig. 8 shows the first Fourier component of the intensity profile along the y direction as a function of the reduced defocusing distance D/D_T obtained on a pure phase grating with period a = 6.35 μm at λ = 0.69 Å. When the vertical monochromator is used (filled squares) the periodic variation with D is damped. The decrease in contrast is due to the partial coherence of the incident beam. From the decrease the effective source size is determined to be 200 μm, whereas no clear decrease is visible when the non-vibrating horizontal monochromator is used (filled circles).

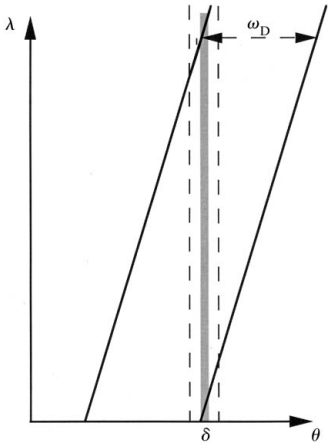

Figure 7
DuMond diagram corresponding to the production of an 18 keV beam at the ID19 beamline using an Si(111) crystal in symmetrical Bragg setting. The dashed region (divergence δ) corresponds to the diffracted beam. A small vibration of the monochromator (1 μrad) widens this region (dashed lines) and decreases the beam coherence when integrated over time.

4. Conclusions

The use of coherence in X-ray imaging opens up possibilities for new physics. Whereas qualitative phase-contrast imaging has been proved to be possible using a microfocus X-ray generator (Wilkins *et al.*, 1996), the high-quality images and the quantitative measurements of coherent phenomena require a third-generation synchrotron radiation facility monochromatic coherent beam. These experiments imply that, in addition, the coherence has been preserved and spurious images have been avoided, at all levels of the beamline. The commissioning of the 'long' ID19 beamline of the ESRF gave the opportunity, due to its sensitivity to coherence effects, of identifying the problems and possible solutions. Similar problems are to be encountered by the other third-generation synchrotron beamlines, presently under commissioning or construction.

We are happy to acknowledge several colleagues from the Topography Group and from the Beamline Project Office (BLPO) of the ESRF for their help during the test experiments. P. Cloetens is indebted to the Fund for Scientific Research of Flanders for financial support.

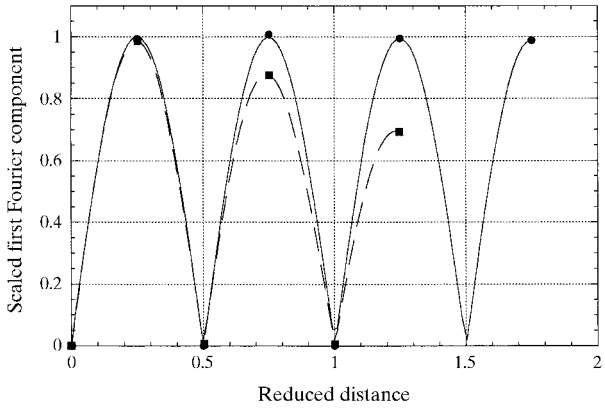

Figure 8
First Fourier component of the intensity profile obtained for a phase grating (period a = 6.35 μm) as a function of the reduced defocusing distance with the beam monochromated by the vertical monochromator (filled squares) or the horizontal monochromator (filled circles). The lines of the grating were horizontal; X-ray energy 18 keV.

References

Authier, A. (1997). *X-rays and Neutrons Dynamical Diffraction: Theory and Applications*, edited by A. Authier, S. Lagomarsino & B. K. Tanner, pp. 1–31. New York: Plenum.

Baruchel, J., Draperi, A. & Zontone, F. (1993). *J. Phys. D*, **26**, A9–A14.

Brauer, S., Stephenson, G.-B., Sutton, M., Brüning, R., Dufresne, E., Mochrie, S.-G.-J., Grübel, G., Als-Nielsen, J. & Abernathy, D.-L. (1995). *Phys. Rev. Lett.* **74**, 2010–2013.

Brauer, S., Stephenson, G.-B., Sutton, M., Mochrie, S.-G.-J., Dierker, S.-B., Fleming, R.-M., Pindak, R., Robinson, I.-K., Grübel, G., Als-Nielsen, J. & Abernathy, D. (1995). *Rev. Sci. Instrum.* **66**, 1506–1509.

Buffière, J.-Y., Maire, E. & Peix, G. (1997). Private communication.

Cloetens, P., Barrett, R., Baruchel, J., Guigay, J.-P. & Schlenker, M. (1996). *J. Phys. D*, **29**, 133–146.

Cloetens, P., Guigay, J.-P., de Martino, C., Baruchel, J. & Schlenker, M. (1997). *Opt. Lett.* **22**, 1059–1061.

Cloetens, P., Guigay, J.-P., de Martino, C., Salomé, M., Schlenker, M. & Van Dyck, D. (1997). *Proc. SPIE*, **3154**, 72–82.

Cloetens, P., Pateyron-Salomé, M., Buffière, J.-Y., Peix, G., Baruchel, J., Peyrin, F. & Schlenker, M. (1997). *J. Appl. Phys.* **81**, 5878–5886.

Guigay, J.-P. (1971). *Opt. Acta*, **18**, 677–682.

Guigay, J.-P. (1977). *Optik*, **49**, 121–125.

Labiche, J.-C., Segura-Puchades, J., Van Brussel, D. &. Moy, J. P. (1996). *ESRF Newsl.* **25**, 41–43.

Pogany, A., Gao, D. & Wilkins, S. W. (1997). *Rev. Sci. Instrum.* **68**, 2774–2782.

Schelokov, I., Hignette, O., Raven, C., Snigireva, I., Snigirev, A. & Souvorov, A. (1996). *Proc. SPIE*, **2805**, 282–292.

Snigirev, A., Snigireva, I., Kohn, V. & Kuznetsov, S. (1996). *Nucl. Instrum. Methods*, A**370**, 634–640.

Snigirev, A., Snigireva, I., Kohn, V., Kuznetsov, S. & Schelokov, I. (1995). *Rev. Sci. Instrum.* **66**, 5486–5492.

Sutton, M., Mochrie, S.-G.-J., Greytak, T., Nagler, S.-E., Berman, L.-E., Held, G.-A. & Stephenson, G.-B. (1991). *Nature (London)*, **352**, 608–610.

Wilkins, S. W., Gureyev, T. E., Gao, D., Pogany, A. & Stevenson, A. W. (1996). *Nature (London)*, **384**, 335–338.